



Exploring the Central Region of NGC 1365 in the Ultraviolet Domain

Kshama Sara Kurian^{1,2}, C. S. Stalin¹, Dominika Wylezalek³, Mariya Lyubenova⁴, Tek Prasad Adhikari^{5,6}, Ashish Devaraj⁷, Ram Sagar¹, Markus Kissler-Patig⁸, and Santanu Mondal¹

¹Indian Institute of Astrophysics, Koramangala, Block II, Bangalore 560034, India; stalin@iiap.res.in

²Pondicherry University, Kalapet, Puducherry 605014, India

³Astronomisches Rechen-Institut, Zentrum für Astronomie der Universität Heidelberg, Monchhofstr. 12-14, 69120 Heidelberg, Germany

⁴European Southern Observatory, Karl-Schwarzschild-Str. 2, 85748 Garching bei München, Germany

⁵CAS Key Laboratory for Research in Galaxies and Cosmology, Department of Astronomy, University of Science and Technology of China, Hefei, Anhui 230026, People's Republic of China

⁶School of Astronomy and Space Science, University of Science and Technology of China, Hefei, Anhui 230026, People's Republic of China

⁷Department of Physics and Electronics, CHRIST (Deemed to be University), Bangalore 560029, India

⁸ESA—ESAC—European Space Agency, Camino Bajo del Castillo s/n, 28692 Villafranca del Castillo, Madrid, Spain

Received 2023 April 30; revised 2024 August 4; accepted 2024 August 4; published 2024 October 3

Abstract

Active galactic nuclei (AGN) feedback and its impact on their host galaxies are critical to our understanding of galaxy evolution. Here, we present a combined analysis of new high resolution ultraviolet (UV) data from the Ultraviolet Imaging Telescope (UVIT) on AstroSat and archival optical spectroscopic data from the Very Large Telescope/MUSE, for the Seyfert galaxy, NGC 1365. Concentrating on the central 5 kpc region, the UVIT images in the far- and near-UV show bright star-forming knots in the circumnuclear ring as well as a faint central source. After correcting for extinction, we found the star formation rate (SFR) surface density of the circumnuclear 2 kpc ring to be similar to other starbursts, despite the presence of an AGN outflow, as seen in [O III] 5007 Å. On the other hand, we found fainter UV and thus lower SFR in the direction southeast of the AGN relative to northwest in agreement with observations at other wavelengths from JWST and Atacama Large Millimeter/submillimeter Array. The AGN outflow velocity is found to be lesser than the escape velocity, suggesting that the outflowing gas will rain back into the galaxy. The deep UV data have also revealed diffuse UV emission in the direction of the AGN outflow. By combining [O III] and UV data, we found the diffuse emission to be of AGN origin.

Unified Astronomy Thesaurus concepts: Seyfert galaxies (1447); Ultraviolet astronomy (1736); Active galactic nuclei (16); AGN host galaxies (2017)

1. Introduction

Most galaxies in the Universe harbor supermassive black holes (SMBHs; 10^6 – $10^{10} M_{\odot}$) at their centers (Kormendy & Richstone 1995; Kormendy & Ho 2013). These SMBHs, while accreting matter from their surroundings, lead to the trigger of the active galactic nuclei (AGN) as well as the growth of the host galaxy. This close relationship between AGN and host galaxy is also evident in the correlation observed between the mass of the SMBH (M_{BH}) in AGN and galaxy luminosity (Kormendy & Richstone 1995), M_{BH} and galaxy mass (Magorrian et al. 1998), and M_{BH} and the velocity dispersion σ of the stellar bulge (M – σ relation; Ferrarese & Merritt 2000). AGN thus play an important role in the evolution of galaxies via the injection of energy into the gas in their host galaxies, a process called feedback (Fabian 2012; King & Pounds 2015).

In many AGN, nuclear outflows from their central regions, in both ionized and molecular phases, have been observed, and these outflows can have a strong impact on the formation of stars in the central regions of AGN. They can either suppress star formation (SF; negative feedback; Maiolino et al. 2012; Harrison 2017) or enhance star formation (positive feedback; Zubovas et al. 2013; Nesvadba et al. 2020). Also, both positive and negative feedback can operate in the same system (Shin et al. 2019; García-Bernet et al. 2021). A clear understanding

of the impact AGN have on the central regions of their host galaxies requires high-resolution observations such as those from integral field spectroscopy (IFS), which can spatially resolve SF and AGN outflows. Such high-resolution observations have become possible in recent years. However, combining such high spatial resolution observations, along with observations at other wavelengths such as submillimeter/UV and photoionization modeling would be a robust and better approach to establishing how the connection between SF and AGN works. At low redshifts, dominated by Seyfert-type AGN, we can spatially separate the AGN-dominated regions from the SF-dominated regions. Here we report the results of one such study on a nearby AGN NGC 1365.

NGC 1365 is a low-luminosity ($L_{\text{bol}} = 2 \times 10^{43} \text{ erg s}^{-1}$) Seyfert 1.8-type AGN at a distance of 18.6 Mpc (Alonso-Herrero et al. 2012; Lindblad 1999). At this distance, $1''$ corresponds to about 90 pc. An early comprehensive review of the characteristics of the AGN in NGC 1365 can be found in Lindblad (1999). It is found to show biconical ionized outflows in [O III] (Phillips et al. 1983; Lena et al. 2016; Venturi et al. 2018). Star-forming clusters have also been found in the central regions of NGC 1365 from infrared observations (Alonso-Herrero et al. 2012; Fazeli et al. 2019; Liu et al. 2023; Whitmore et al. 2023) and X-ray studies (Wang et al. 2009). This source has been extensively studied at high spatial resolution in the optical using IFS data from the Very Large Telescope/MUSE (Venturi et al. 2018) and optical spectra from TYPHOON (Sextl et al. 2024), in the infrared using Herschel (Sandqvist et al. 2021), in the near- and mid-infrared

using JWST (Liu et al. 2023; Schinnerer et al. 2023; Whitmore et al. 2023) as well as in the submillimeter using Atacama Large Millimeter/submillimeter Array (ALMA; Gao et al. 2021; Schinnerer et al. 2023). Although NGC 1365 is well studied in nearly all wavelength domains, the UV domain is unexplored. We aim to fill this gap and explore the relation between the AGN outflow and SF in the central 5 kpc² region (hereafter referred to as the “inner region”) of the galaxy using spatially resolved optical IFS data and newly acquired UV data from the Ultraviolet Imaging Telescope (UVIT) on board AstroSat (Agrawal 2006; Singh 2022), which is India’s first space-based multiwavelength astronomical observatory.

2. Observations

2.1. UVIT

NGC 1365 was observed using UVIT in two broadband filters, namely F169M (far-ultraviolet (FUV); $\lambda_{\text{mean}} = 1608 \text{ \AA}$, $\Delta\lambda = 290 \text{ \AA}$) and N279M (near-ultraviolet (NUV); $\lambda_{\text{mean}} = 2792 \text{ \AA}$, $\Delta\lambda = 90 \text{ \AA}$) (Tandon et al. 2017). UVIT has a spatial resolution better than $1''.5$ and covers a field of view of $\sim 28'$ diameter. The observations (PI: G. Dewangan) were done in the photon counting mode with a default frame count rate of ~ 29 frames per second (Tandon et al. 2017). We downloaded the science-ready level-2 (L2) images that correspond to the OBSIDs A02_006T01_9000000776, A02_006T01_9000000802 and A02_006T01_9000000934 from the Indian Space Science Data Center (ISSDC), Bangalore. In the combined images from ISSDC, we found the exposure time to be lesser than the sum of the individual orbit-wise images. We, therefore, based our analysis on the reduced orbit-wise images. We first aligned the orbit-wise images using the Image Reduction and Analysis Facility (Tody 1986) and combined those aligned orbit-wise images to create the combined images filter-wise. The net exposure times of the resulting images are 24905 s and 37833 s in F169M and N279M filters, respectively. Astrometry on the combined images was carried out using the `astrometry.net` package (Lang et al. 2010). The UVIT position of the AGN matches within $0''.7$ of the Gaia position. For NGC 1365 observations, the background in FUV and NUV is 1×10^{-4} cps/arcsec² and 2.2×10^{-4} cps/arcsec², respectively. The top panel of Figure 1 shows the composite image of NGC 1365 in FUV (blue) and NUV (red). Bright FUV and NUV knots of SF are seen in the inner region and the spiral arms. The bottom panel of Figure 1 shows the zoomed-in view of the FUV and NUV flux maps of the inner region that covers the MUSE field of view.

2.2. MUSE

The MUSE optical Integral Field Unit (IFU) observations of NGC 1365 were acquired on 2014 October 12 under the program 094.B-0321(A) (PI: A. Marconi; Venturi et al. 2018). For our data analysis, we used the fully reduced, 4 ks deep data cube of NGC 1365, which is available on the ESO archive. The MUSE field of view is $1' \times 1'$ with a $0''.2$ pixel⁻¹ spatial sampling. The median seeing during the observations was about $0''.76$ (Venturi et al. 2018). The spectral window is 4750–9352 Å, and the spectral binning is 1.25 Å per channel.

3. Data Analysis

3.1. MUSE

We analyzed the MUSE data using a combination of our own Python scripts and the Python package MUSE Python Data Analysis Framework (Bacon et al. 2016). The central $2''$ nuclear region was not considered for further analysis as we are not interested in the broad line region of NGC 1365. To estimate the host galaxy kinematics, we fitted a single Gaussian to the Ca+Fe blend (MUSE resolution allows the blend to be treated as a single line) at 6495 Å (Ho et al. 2009), after subtracting the stellar continuum. For this, spaxels with signal-to-noise ratio (SNR) > 3 were considered. Here, SNR is the ratio of the absolute value of the flux to the standard deviation of the line-free region of the continuum-subtracted spectra. In the top left panel of Figure 2 we show the rotational velocity of the inner region of NGC 1365 as derived from the Ca+Fe blend. This is similar to that derived by Venturi et al. (2018) using the Penalized Pixel-fitting (Cappellari & Emsellem 2004) code.

We measure the flux of the [S II] doublet at $\lambda 6716, 6731 \text{ \AA}$, H β —[O III] line complex (H β — $\lambda 4861 \text{ \AA}$, [O III] doublet— $\lambda 4959, 5007 \text{ \AA}$), and H α —[N II] line complex (H α — $\lambda 6564.6 \text{ \AA}$, [N II] doublet— $\lambda 6549.8, 6585.2 \text{ \AA}$). To estimate the flux of the emission lines, we fitted each individual observed emission line with two Gaussian components (except for H β and H α , which required an additional Gaussian component to account for the absorption line) that reproduces the line profile well. During the fit, the intensity ratios of the [O III] and [N II] doublets were fixed to 2.95 and 3.0, respectively (Osterbrock & Ferland 2006). To separate shocked or low-ionization nuclear emission-line (LINER) regions from AGN or Seyfert and starburst ionized gas, we used the [S II]-Baldwin, Phillips, and Terlivich (BPT; Baldwin et al. 1981; Veilleux & Osterbrock 1987) diagram ([S II]6716, 6731/H α versus [O III]5007/H β). The BPT diagram indicates that the conical [O III] 5007 Å emission seen in the inner region of NGC 1365 is predominately due to photoionization from AGN and is confined to the northwest (NW) and southeast (SE) directions.

We determined the kinematics of the [O III] emission line using the V50 and W80 parameters (Zakamska & Greene 2014) from the total fitted line profile of the [O III] 5007 Å line. The parameter V50 is the velocity at 50% of the total flux and is a proxy to the velocity shift. W80 is the difference between the 90th and 10th percentiles of the total flux and is a proxy to the velocity dispersion (W80 = 1.088FWHM; Zakamska et al. 2016). Figure 2, top right and bottom left panels, show the kinematic maps derived from the [O III] 5007 Å line. The AGN photoionized cone is clearly seen to be outflowing in the [O III] 5007 Å velocity shift map after subtraction of the stellar rotational velocity. The NW cone is redshifted, while the SE cone is blueshifted. We found the AGN ionization cone to have high W80 values of greater than 450 km s⁻¹.

We estimated the color excess $E(B - V)$ as

$$E(B - V) = 1.97 * \log_{10} \left[\frac{(H_{\alpha}/H_{\beta})_{\text{obs}}}{(H_{\alpha}/H_{\beta})_{\text{int}}} \right], \quad (1)$$

where $(H_{\alpha}/H_{\beta})_{\text{obs}}$ and $(H_{\alpha}/H_{\beta})_{\text{int}}$ are the observed and intrinsic H α /H β line ratio, respectively. This equation considers an intrinsic value for (H_{α}/H_{β}) to be 2.87 under Case B recombination conditions (Osterbrock & Ferland 2006).

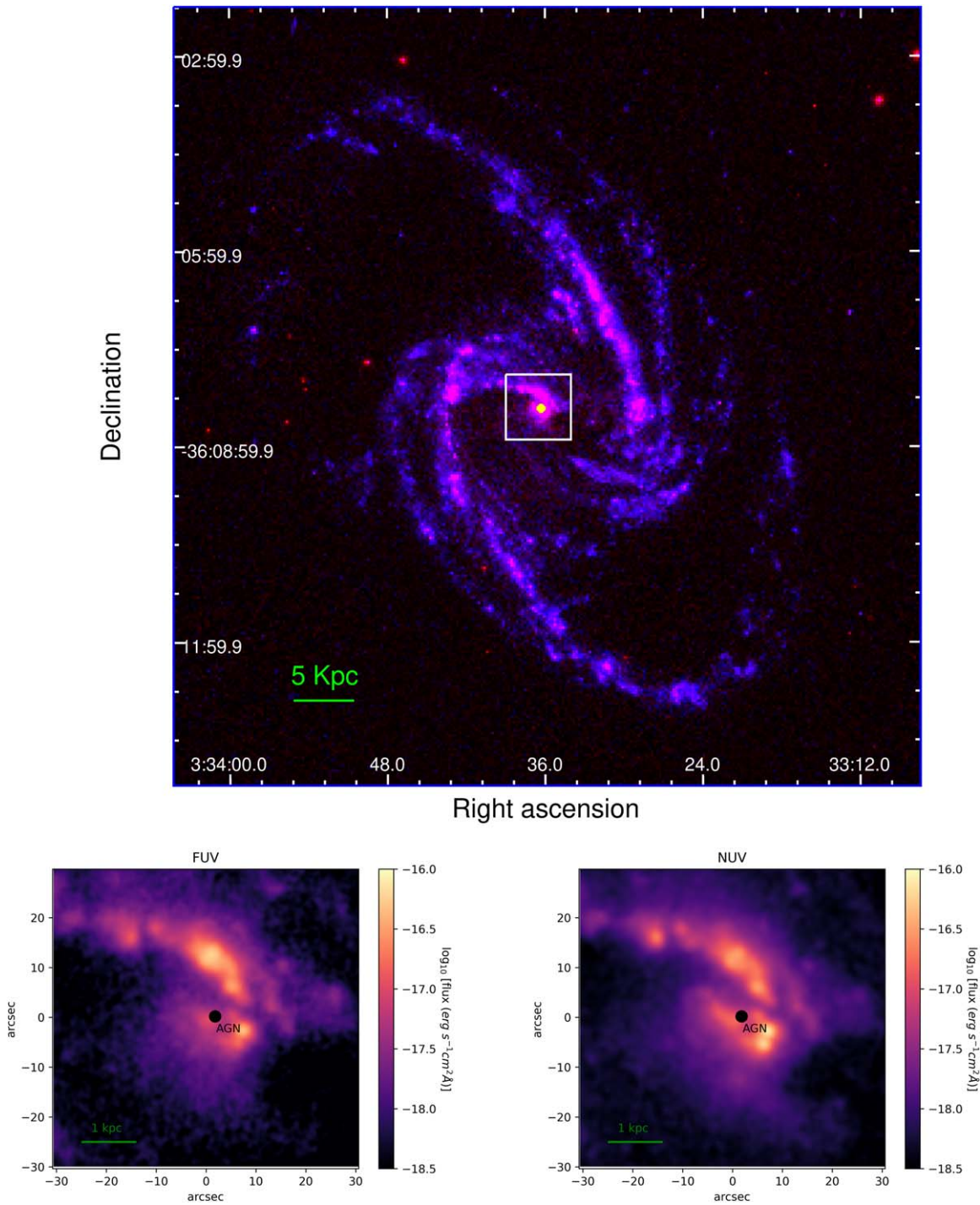


Figure 1. Top panel: composite UVIT image of NGC 1365 with FUV in blue and NUV in red. The white box is the MUSE field of view ($\sim 1' \times 1'$) corresponding to the central 5 kpc region, which is the region analyzed in this work. The yellow dot in the center of the box is the AGN position. Bottom panels: the UVIT FUV (left) and NUV (right) images of the inner 5 kpc region of NGC 1365 corresponding to the MUSE field of view. They have been corrected for Milky Way extinction. The black dot in the center of the NUV and FUV images is the AGN position.

Figure 2, bottom right panel, shows the $E(B - V)$ map of the nebular gas. We found the ring to have an average $E(B - V)$ of ~ 1 , which translates to an A_V of ~ 3 (assuming $R_V = 3.1$) and is similar to that found by Venturi et al. (2018).

3.2. UVIT

The UVIT FUV and NUV images were converted to flux units using the unit conversion in Tandon et al. (2017). In order to perform a combined study of the MUSE and UVIT data, the

UVIT FUV and NUV images of NGC 1365 were cropped to the MUSE field of view. The position of the AGN in UVIT matches with the MUSE position within $0''.4$. We then corrected the UV data for the Galactic extinction using Cardelli et al. (1989), for a foreground extinction at the V band of 0.0543 mag, taken from Schlafly & Finkbeiner (2011). The intrinsic FUV and NUV fluxes were then estimated from the Milky Way-corrected UV fluxes applying the Calzetti et al. (2000) reddening curve for the wavelength range,

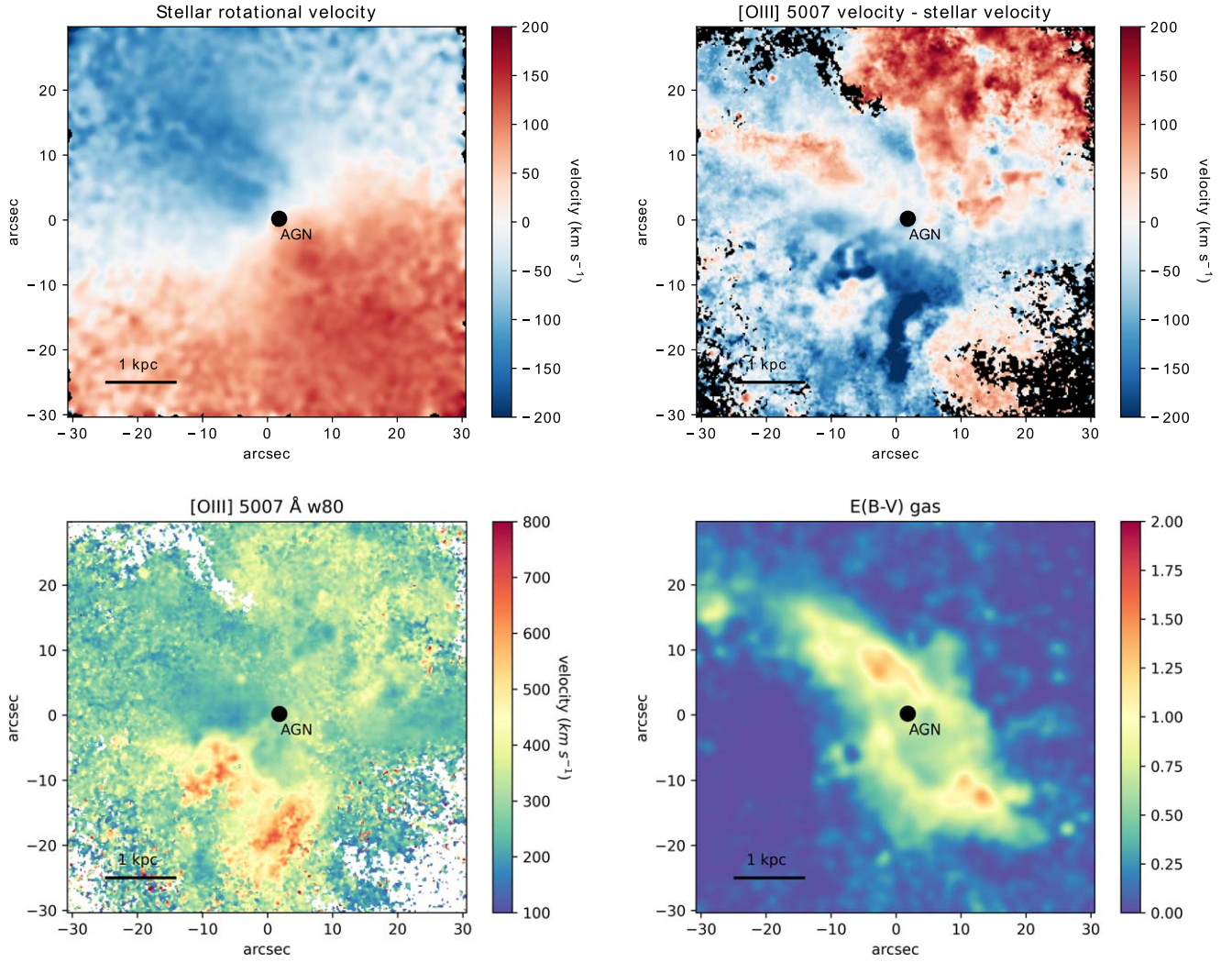


Figure 2. The stellar rotational velocity map (top left), the stellar rotational velocity subtracted [O III] 5007 Å velocity shift (top right), the W80 map of the [O III] 5007 Å line (bottom left), and the $E(B - V)$, of the nebular gas (bottom right). The AGN is marked based on the brightest $H\alpha$ region showing broad $H\alpha$ emission-line width.

$1200 \text{ \AA} \leq \lambda \leq 6300 \text{ \AA}$, which is

$$k_\lambda = 2.65 \left(-2.15 + \frac{1.50}{\lambda} - \frac{0.19}{\lambda^2} + \frac{0.01}{\lambda^3} + R_v \right). \quad (2)$$

Here, $R_v = 3.1$. Following Calzetti et al. (2000), we estimated the color excess of the stellar emission from the color excess of the nebular emission using $E_s(B - V) = 0.44E(B - V)$. We then calculated the intrinsic UV flux using the equation,

$$F_{\text{int}}(\lambda) = F_{\text{obs}}(\lambda) 10^{0.4E_s(B-V)k_\lambda}. \quad (3)$$

4. Results

4.1. UV Slope— β

The UV continuum slope is a proxy to the UV color from which age and other stellar population characteristics can be derived (Calzetti 2001). The UV slope β is defined as the slope of the power-law function, $F_\lambda \propto \lambda^\beta$, where F_λ is the flux density. We created a map of the observed and intrinsic (extinction-corrected) UV slope, β , which is shown in Figure 3.

The intrinsic β map shows the star-forming regions in green with negative β values. The deepest green regions have β values close to -2.5 , which is the dust-free β value of a 5 Myr stellar population, assuming an instantaneous burst of SF and solar abundance (refer to Table 6 in Calzetti 2001).

4.2. Star Formation Rate

There are several star formation rate (SFR) estimates in the literature for the central regions of NGC 1365 (Alonso-Herrero et al. 2012; Fazeli et al. 2019; Gao et al. 2021). They mainly use $H\alpha$ flux values, which is an indirect estimator of SFR. On the contrary, UV flux directly traces the radiation from young star-forming regions and thus is the most appropriate estimator of SFR. Using the high-resolution, extinction-corrected UVIT FUV and NUV data, we derived new estimates of SFR. Most of the SF is said to be taking place in the inner Lindblad region (Galliano et al. 2005), mainly concentrated in a star-forming ring of approximate diameter 2 kpc (Alonso-Herrero et al. 2012). We estimated the intrinsic FUV and NUV SFR for the central $12''$ radius region after masking the central $2''$ radius region, which is dominated by AGN light. We estimated the

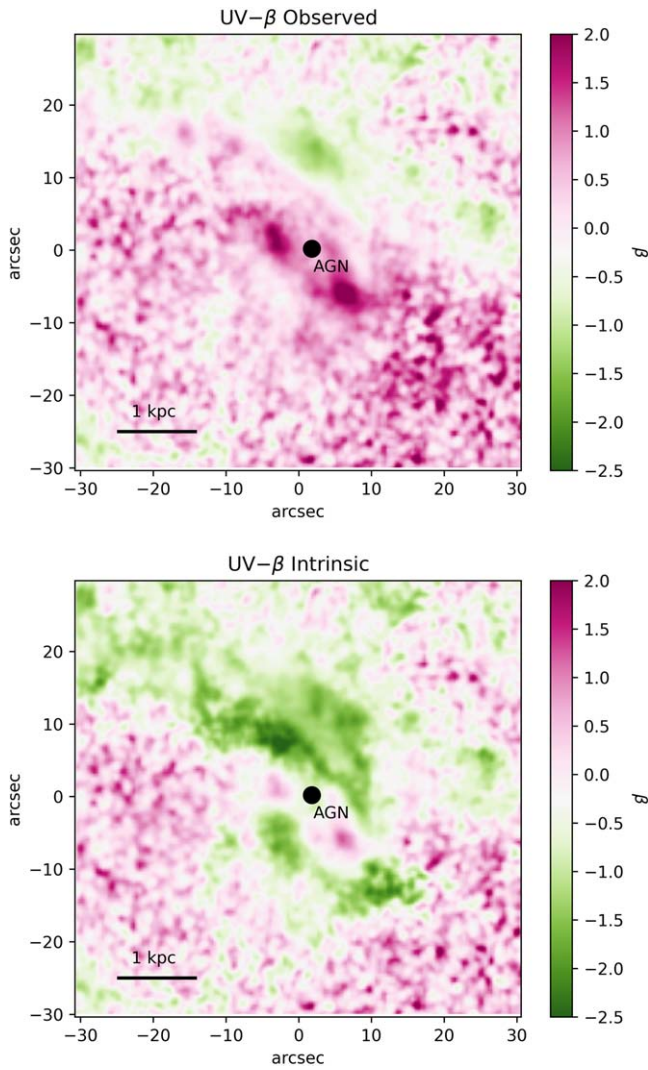


Figure 3. Map of the observed (top) and intrinsic (extinction-corrected, bottom) UV slope, β , of the inner region of NGC 1365. The extinction-corrected β map shows negative β values (green colored) in the regions predominantly occupied by massive SF as seen in the $H\alpha$ map in Venturi et al. (2018).

SFR using the following equation from Calzetti (2013), assuming a Kroupa IMF:

$$\text{SFR} = 3 \times 10^{-47} \lambda L_{\lambda} (M_{\odot} \text{ yr}^{-1}). \quad (4)$$

The UV SFRs are highly dependent on extinction correction, and so, to be thorough, we estimated the SFR for the Calzetti et al. (2000) reddening curve, with a starburst $R_v = 4.05$ and 3.1, the Small Magellanic Cloud (SMC) attenuation curve (Gordon et al. 2003), and the Milky Way reddening curve (Cardelli et al. 1989). For comparison, we also estimated the SFR from $H\alpha$ flux values. Both the UV and $H\alpha$ SFRs are shown in Table 1. Alonso-Herrero et al. (2012) estimated an SFR of $5.6 M_{\odot} \text{ yr}^{-1}$ from $H\alpha$ and Spitzer $24 \mu\text{m}$ IR flux, for a Salpeter IMF. We also derived the SFR surface density of NGC 1365 for a radius of 900 pc. It is found to be between 0.76 and $2.94 M_{\odot} \text{ yr}^{-1} \text{ kpc}^{-2}$ for SFR estimated from FUV and between 1.72 and $2.53 M_{\odot} \text{ yr}^{-1} \text{ kpc}^{-2}$ for SFR estimated from NUV, assuming the various attenuation curves. This is well within the expected SFR surface density at 1 kpc scale from the center of

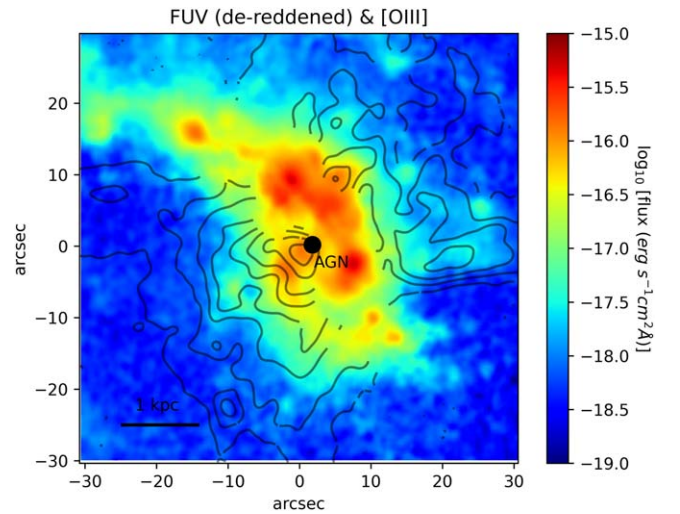


Figure 4. Extinction-corrected, intrinsic UVIT FUV flux map of the inner region of NGC 1365, with MUSE [O III] 5007 Å contours overlaid in black. Only the AGN-dominated regions are shown in the [O III] contours after masking the LINER- and starburst-dominated regions using the [S II]-BPT diagram.

Table 1

SFR of the Bright Star-forming Ring in the Central Region of Diameter 2.2 kpc of NGC 1365 ($r = 12''$, $1'' \sim 90$ pc, Kroupa IMF)

Attenuation Law	SFR FUV ($M_{\odot} \text{ yr}^{-1}$)	SFR NUV ($M_{\odot} \text{ yr}^{-1}$)	SFR $H\alpha$ ($M_{\odot} \text{ yr}^{-1}$)
Uncorrected	0.22	0.82	0.60
Starburst, $R_v = 3.1$	2.68	4.76	3.12
Starburst, $R_v = 4.05$	3.66	6.34	6.41
Milky Way	1.90	4.40	3.51
SMC	7.37	4.31	2.67

the galaxy for other starbursts (Kennicutt 1998; Valencia-S. et al. 2012).

4.3. Spatial Variation in SFR

In Figure 4, we show the extinction-corrected (following Calzetti et al. 2000 with $R_v = 3.1$) intrinsic FUV and NUV SFR map of the inner region with the [O III] 5007 Å AGN outflow contours overlaid in black. The starburst- and LINER-dominated regions have been masked in the [O III] outflow contours using the [S II]-BPT diagram, and hence the [O III] contours in this image show only the regions that are AGN dominated.

The intrinsic UV flux maps are directly proportional to the spatially resolved SFR in the inner region. In NGC 1365, we found a spatial variation of SFR in the star-forming ring. Specifically, the SE part of the ring has low FUV (lower SFR) with respect to the NW side of the ring. The low SFR regions are cospatial with the regions showing strong [O III] contours in the SE cone, possibly hinting for the outflow affecting the SF. However, star-forming rings seen in galaxies are generally made of several aligned knots of SF, and the SF can also be patchy (Comerón et al. 2010, 2014). Recently, using high-resolution observations of the inner region of NGC 1365 from ALMA and JWST coupled with simulations, Schinnerer et al. (2023) found that the distribution of SF in its

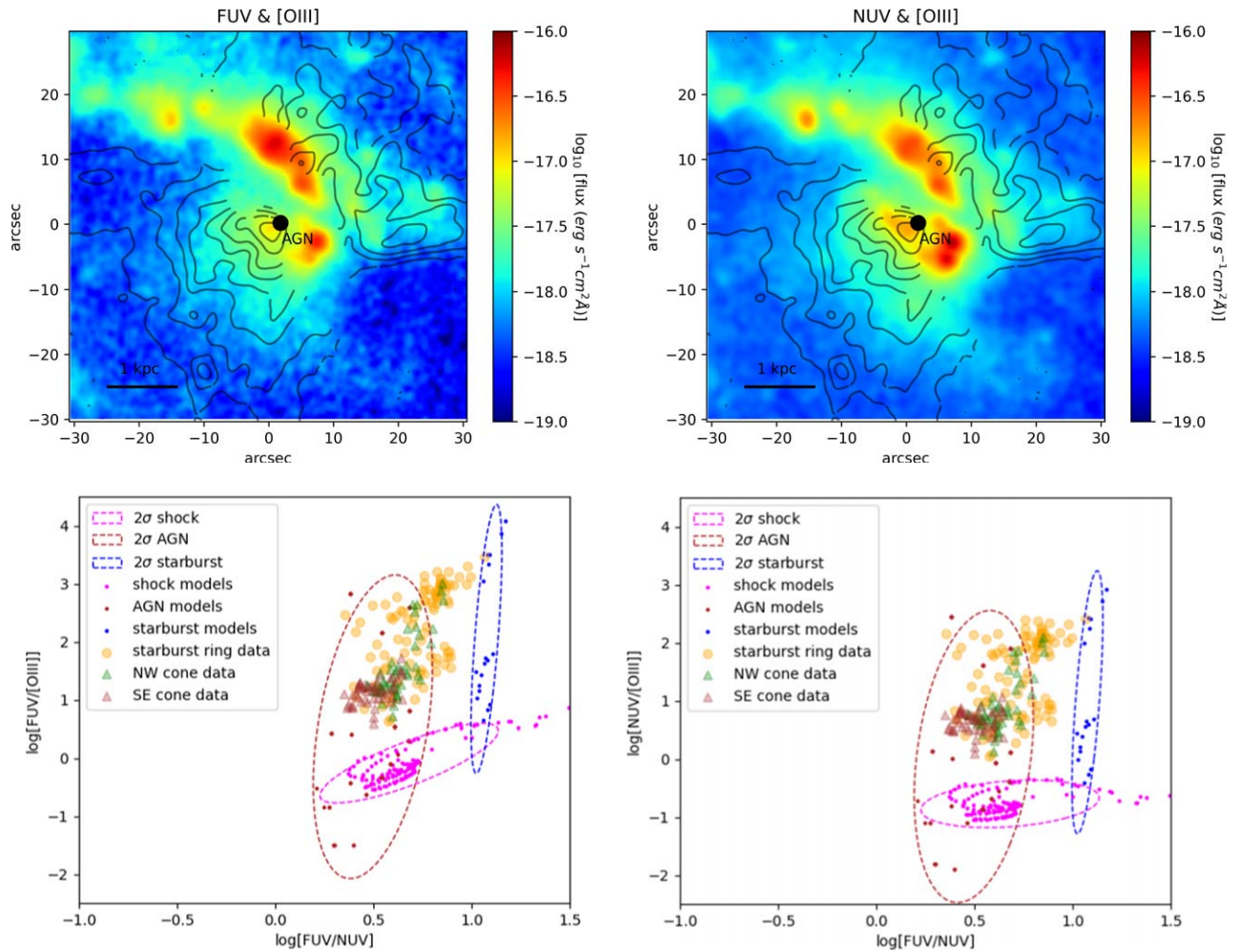


Figure 5. Results from the combined UVIT and MUSE observations. Top panel: Galactic extinction-corrected FUV (left) and NUV (right) maps of the inner region of NGC 1365, with AGN-dominated [O III] 5007 Å contours from MUSE observations overlaid in black. Diffuse FUV and NUV emission is seen cospatial to the [O III] cone both in the NW and SE directions. Bottom panel: flux ratios, FUV/[O III] vs. FUV/NUV (left) and NUV/[O III] vs. FUV/NUV (right) of the starburst (yellow circles), AGN NW cone (green triangles), and AGN SE cone (red triangles) in the inner region of NGC 1365. Model flux ratios of AGN and starburst photoionized gas are shown in red and blue points, and shocked gas is shown in magenta. Confidence ellipses having 95% confidence are drawn around their respective model values.

central region is inhomogeneous. The northern side of the AGN has high SF, while the southern side has reduced SF, though the molecular gas is similar on both the northern and southern sides. According to them, the SF in the central region is driven by gas inflow via bar, and SF in the southern regions has not yet started. They conclude that the AGN outflow thus has no impact on the gaseous disk. Considering the inclination of the AGN outflow and the galactic disk, the SE cone is above the disk, with its axis 5° within the galaxy axis (Hjelm & Lindblad 1996). Hence it seems less likely to intersect the galaxy plane. From studies of molecular gas kinematics, Liu et al. (2023) too do not find evidence of the ionized outflow to intersect the molecular gas disk. Recent high-resolution observations are thus not in agreement with the scenario proposed by Gao et al. (2021), wherein the outflow impacts the molecular disk and causes AGN feedback, based on poor-resolution ALMA maps. From UVIT observations, we found fainter UV and thus lower SFR in the SE side relative to the NW side of the AGN, which is in agreement with the recent high-resolution observations from JWST and ALMA (Liu et al. 2023; Schinnerer et al. 2023; Whitmore et al. 2023).

4.4. Diffuse UV Light Observed in the Outflow Cone

The UV morphology of the central regions of NGC 1365 predominantly points to a starburst origin of UV light when compared with the $H\alpha$ flux map. Along with the bright starburst regions, there is diffuse UV light in the NW and SE sides of the AGN-dominated cone, which are, in parts, similar to the morphology seen in the [O III] outflow. This is shown in the Galactic extinction-corrected UV images in the top panel of Figure 5.

To determine the origin of this diffuse UV light, which is cospatial with the [O III] outflow region, we compared UV and [O III] flux values to shock and photoionization models. We first calculated the flux ratios of FUV/[O III], NUV/[O III], and FUV/NUV for the outflow and the starburst ring of NGC 1365 after smoothing the [O III] line emission map (by convolving with a Gaussian) to match the spatial resolution of UVIT data. To estimate the flux ratios, we used the Calzetti et al. (2000) ($R_V = 3.1$) extinction-corrected FUV and NUV fluxes multiplied with their respective bandwidths ($\Delta\lambda = 290 \text{ \AA}$ for FUV and $\Delta\lambda = 90 \text{ \AA}$ for NUV). The starburst region was taken to be the same as the area used to determine the SFR in Section 4.2.

This region was divided into smaller regions, and the mean flux ratio in each section was calculated. The outflow region was roughly ascertained to be a double cone centered at the AGN, having a full opening angle of 90° , by using the [S II]-BPT AGN mask. This value of the opening angle is within the maximum opening angle of 100° modeled by Hjelm & Lindblad (1996).

We then estimated AGN and starburst photoionization as well as shock model flux ratios. The model values of the gas photoionized by AGN and starburst were generated using CLOUDY 17.0 (Ferland et al. 2017). For the AGN photoionization model, we considered a standard AGN continuum, with a big blue bump (BBB) temperature of 10^5 K, an X-ray to UV slope of $\alpha_{ox} = -1.5$, a low-energy BBB slope of $\alpha_{uv} = -0.5$, and an X-ray power-law index of $\alpha_x = -1.35$ (Guainazzi et al. 2009). We computed the AGN models under isobaric conditions assuming plane parallel geometry (Adhikari et al. 2018), with an initial pressure of $P = 2 \times 10^7$ K (D’Agostino et al. 2018). We adopted Milky Way dust grain abundance for solar metallicity. We generated a grid of spectra for photoionized gas, spanning a large range in ionization parameter: $\log(U) = [-3.5, 2.0]$, hydrogen density $\log(n_H) = [3, 6]$ (these are typical densities of the AGN narrow line region), and total column density $\log(N_H) = [19, 24]$. For the starburst models, we generated spectra of spherical H II regions photoionized by instantaneous starburst continuum whose spectra with stellar masses that span the range between $1 M_\odot$ and $100 M_\odot$ were taken from Starburst99 (Leitherer et al. 1999) for ionization parameter: $\log(U) = [-4.0, -2.0]$, hydrogen density $\log(n_H) = [1, 3]$, and starburst ages of 1 and 5 Myr. Similar to the AGN models, we adopted Milky Way dust grain abundance for solar metallicity for the starburst models.

The shock models were generated from MAPPINGS III (Allen et al. 2008) for shock velocities of $100\text{--}1000$ km s $^{-1}$, assuming preshock gas densities of $0.1\text{--}1$ cm $^{-3}$ and magnetic field values of $1\text{--}10$ μ G. We then compared the extinction-corrected flux ratios (applying reddening curve by Calzetti et al. (2000), for an $R_v = 3.1$) to AGN photoionization, starburst photoionization, and shock model predictions. Figure 5, bottom panel, shows the flux ratio map of FUV/[O III] versus FUV/NUV and NUV/[O III] versus FUV/NUV.

The flux ratios, FUV/[O III] and NUV/[O III], of the outflow region, along with their FUV/NUV values, are found to match with AGN models. This indicates that the diffuse UV emission in the outflow region is predominantly of AGN origin. This could be due to line emission from AGN photoionization of gas clouds in the outflow (Feltre et al. 2016) as well as direct and scattered AGN continuum light from electrons or dust in the outflow (Zakamska et al. 2005; Obied et al. 2016).

Geometrically, the outflow cone is said to have an opening angle of 100° (Hjelm & Lindblad 1996) or a half-opening angle of 50° with an inclination from line of sight of 40° (Jorsater & van Moorsel 1995). From modeling the torus, Alonso-Herrero et al. (2012) estimated an opening angle 36° . Since the torus is thought to confine the outflow opening angle, this value suggests a narrower cone. If we assume the outflow cone half-opening angle of the SE cone is 36° and is inclined at 40° from the line of sight, this would limit the contribution from the direct AGN continuum. However, it is possible for electrons or dust in the cone to scatter the AGN continuum. Alternatively, there can also be a contribution from two-photon decay and

hydrogen fluorescence to diffuse UV emission (Kulkarni 2022). The fact that the diffuse emission is detected in both FUV and NUV, as well as in both the southern and part of the northern cones, may provide the strongest support to the scattered light origin. This is also in accord with the results found by Zakamska et al. (2005) and Obied et al. (2016) in scattering cones of AGN.

Our observations indicate that deep UV data can also be used to reveal scattered light by dust in the AGN outflow. To the best of our knowledge, such a study, combining photometric UV data with spectroscopic [O III] emission, has not been undertaken in Seyfert galaxies, and this is the first study of its kind.

4.5. Impact of AGN Feedback in NGC 1365

From the estimation of the UV SFR surface density, the AGN outflow in NGC 1365 seems to have no impact on the total SFR in the circumnuclear ring as the SFR surface density is comparable to other starbursts. Also, the SFR variation seen in the central ring need not be due to the observed AGN outflow. NGC 1365 is a barred galaxy, and in such galaxies, gas flows into the nuclear rings via the dust lanes. From hydrodynamical simulations it is found that variations in the gas inflow rate can lead to changes in SF in the nuclear ring, including lopsided SF (Sormani et al. 2023). Therefore, inflow has a causal connection in regulating SF in nuclear rings (Sormani et al. 2020; Moon et al. 2021, 2022). Lopsided SF in nuclear rings is known from observations (Callanan et al. 2021). Recent high-resolution observations of NGC 1365, supported by simulations too favor a scenario wherein the varied SFR in the ring is due to gas inflow (Schinnerer et al. 2023). We thus conclude that the ionized AGN outflow has no impact to the molecular gas in the central region of NGC 1365, and thus the observed lopsided SF in the ring on either side of the AGN in NGC 1365 is explainable without invoking AGN feedback (Schinnerer et al. 2023).

The ionized gas in the [O III] outflow has velocities of the order of $100\text{--}150$ km s $^{-1}$. (Venturi et al. 2018; this work). We estimated the escape velocity at 1 kpc to be of the order of 600 km s $^{-1}$ using the equation in Rupke et al. (2002),

$$v_{\text{esc}}(r) = \sqrt{2} v_{\text{circ}} * \left[1 + \ln \left(1 + \frac{r_{\text{max}}}{r} \right) \right]^{0.5}, \quad (5)$$

where $v_{\text{circ}} = \sqrt{2} \sigma_*$ is the circular velocity and $r_{\text{max}} = 100$ kpc (Greene et al. 2011). This was calculated assuming a stellar dispersion σ_* of 120 km s $^{-1}$ for NGC 1365 (Caglar et al. 2020). Thus, though the ionized gas is outflowing, it does not have the energy to escape the host galaxy’s potential. This is similar to the findings of other low- and moderate-luminosity Seyfert galaxies (Davies et al. 2014; Shimizu et al. 2019). The gas would just rain back down into the galaxy and help to relocate gas and dust and chemically enrich the galaxy. A caveat is that the outflow velocities considered here are the projected line-of-sight velocities and are not indicative of true outflow velocities, which may be higher for high inclination angles of the outflow to the line of sight. However, Sextl et al. (2024) find low metallicities in the central region of NGC 1365, which they attribute to a combination of inflow of metal-poor gas and AGN feedback interrupting the SF in the ring. Thus, though the AGN outflow may not escape the host galaxy, it

may have the potential to influence the SF in the vicinity during its active phase.

5. Summary

The work presented here aims to understand the impact of AGN activity on SF in NGC 1365 using new FUV and NUV data from UVIT combined with archival MUSE optical IFU data. The results of the work are summarized below.

1. The UV data confirm existing literature studies of the SFR of the starburst ring in NGC 1365. We estimated an SFR of $2.68 M_{\odot} \text{ yr}^{-1}$ for the central 2 kpc from the FUV flux map corrected for extinction using the Calzetti et al. (2000) attenuation law assuming an R_v of 3.1. The estimated SFR surface densities of NGC 1365 are similar to other starbursts.
2. We found low FUV flux values (and hence low SFR) in the east and SE parts of the star-forming ring (see Figure 4, left panel). This finding based on the new UV observations reported here is in agreement with those found from the very recent high-resolution observations in the infrared and submillimeter from JWST and ALMA. According to Schinnerer et al. (2023), this inhomogeneity in SF characteristics on either side of the AGN is due to differences in the onset of SF.
3. The UV data revealed previously undetected diffuse UV emission cospatial with the [O III] 5007 Å outflow of AGN origin (see Figure 5 top panel). Such a detection was possible only due to deep UV data combined with the high spatial resolution of UVIT. This points to a common origin for [O III] 5007 Å and diffuse UV emission in the northern and southern cones.
4. Ratios of UV fluxes to [O III] continuum-subtracted line fluxes indicate that the diffuse UV emission, which is cospatial with the [O III] 5007 Å outflow, is of AGN origin (see Figure 5, bottom panel). This may be due to

AGN light being scattered by electrons and dust particles in the bicone.

5. We estimated the escape velocity at 1 kpc to be about 600 km s^{-1} . As the projected velocity of the outflowing ionized gas is much lower than the escape velocity at 1 kpc, the gas does not have the energy to escape the host galaxy potential and will rain back into the galaxy.

This work has shown the usefulness of UV in characterizing the SF nature of AGN hosts. While UV data as a direct tracer of SF have been used extensively in SF studies, it has been less explored in the AGN domain. With the advent of JWST, rest-frame UV studies of large statistical data sets will throw new light on the prevalence of AGN feedback and its impact on host galaxies.

Acknowledgments

This publication uses data from the AstroSat mission of the Indian Space Research Organization (ISRO), archived at the Indian Space Science Data Centre (ISSDC). This publication uses UVIT data processed by the payload operations center at IIA. The funding provided by the Alexander von Humboldt Foundation, Germany, is thankfully acknowledged. K.S.K. acknowledges the studentship at the European Southern Observatory, Garching. T.P.A. acknowledges the support of the National Natural Science Foundation of China (grant Nos. 12222304, 12192220, and 12192221).

Facilities: AstroSat (UVIT), VLT:Yepun. UVIT was built in collaboration between IIA, IUCAA, TIFR, ISRO and CSA.

Software: Astropy (Astropy Collaboration et al. 2013, 2018), MPDAF (Bacon et al. 2016), Cloudy 17.0 (Ferland et al. 2017).

Appendix A [O III] and H α Flux Maps

Figure 6 shows the [O III] and H α flux maps we derived from the MUSE IFU data.

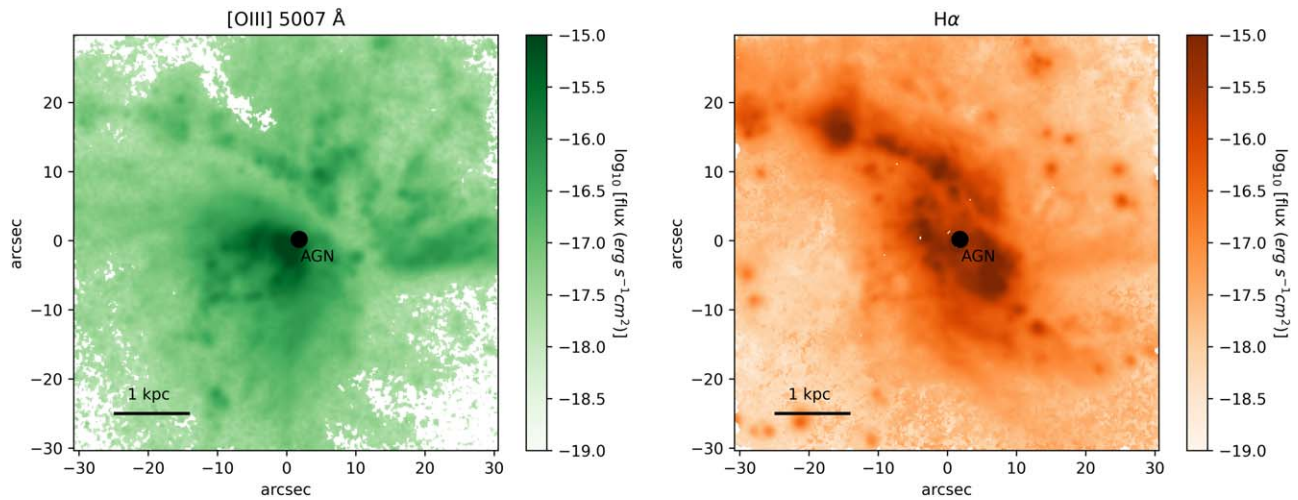


Figure 6. Flux maps of [O III] and H α derived from the MUSE data.

Appendix B Starburst Ring and AGN Double Cone

Figure 7 shows the intrinsic FUV flux map with three regions of interest overlaid, from which the UV-optical flux ratios in Figure 5 have been determined.

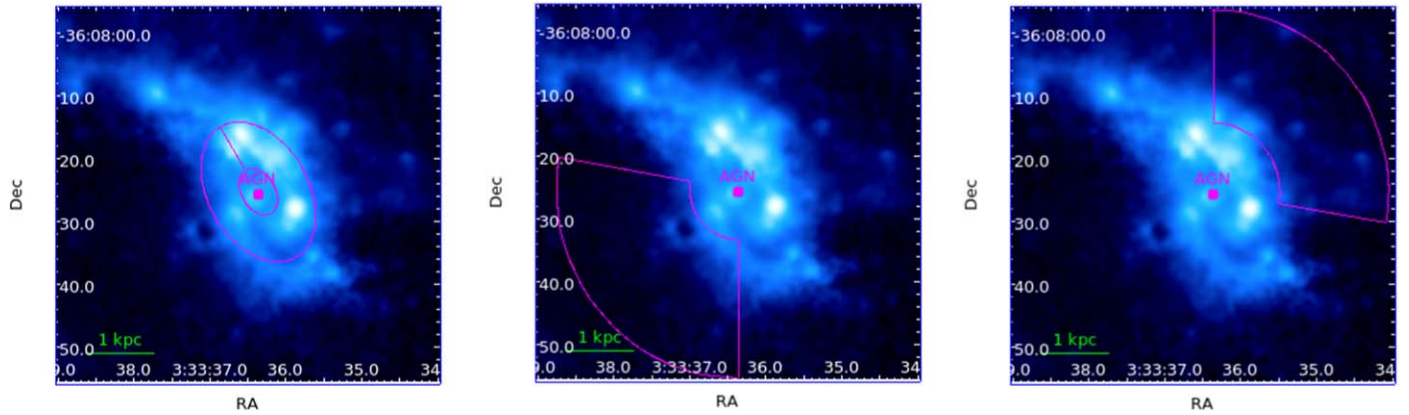











Figure 7. This figure shows the three regions used to determine the UV-optical flux ratios in Figure 5 overlaid on the intrinsic UVIT FUV flux map. The left panel shows the 12'' starburst ring after masking the central AGN. This region is also used to determine the SFR of the ring in Section 4.2. The middle and right panels show the SE and NW cones, respectively.

ORCID iDs

Kshama Sara Kurian  <https://orcid.org/0009-0002-8410-9937>
 C. S. Stalin  <https://orcid.org/0000-0002-4998-1861>
 Dominika Wylezalek  <https://orcid.org/0000-0003-2212-6045>
 Mariya Lyubenova  <https://orcid.org/0000-0002-4381-0383>
 Tek Prasad Adhikari  <https://orcid.org/0000-0003-4586-0744>
 Ashish Devaraj  <https://orcid.org/0000-0001-5933-058X>
 Ram Sagar  <https://orcid.org/0000-0003-4973-4745>
 Markus Kissler-Patig  <https://orcid.org/0000-0002-5908-1488>
 Santanu Mondal  <https://orcid.org/0000-0003-0793-6066>

References

- Adhikari, T. P., Hryniewicz, K., Rózańska, A., Czerny, B., & Ferland, G. J. 2018, *ApJ*, **856**, 78
- Agrawal, P. C. 2006, *AdSpR*, **38**, 2989
- Allen, M. G., Groves, B. A., Dopita, M. A., Sutherland, R. S., & Kewley, L. J. 2008, *ApJS*, **178**, 20
- Alonso-Herrero, A., Sánchez-Portal, M., Ramos Almeida, C., et al. 2012, *MNRAS*, **425**, 311
- Astropy Collaboration, Price-Whelan, A. M., Sipőcz, B. M., et al. 2018, *AJ*, **156**, 123
- Astropy Collaboration, Robitaille, T. P., Tollerud, E. J., et al. 2013, *A&A*, **558**, A33
- Bacon, R., Piqueras, L., Conseil, S., Richard, J., & Shepherd, M. 2016, MPDAF: MUSE Python Data Analysis Framework, Astrophysics Source Code Library, ascl:1611.003
- Baldwin, J. A., Phillips, M. M., & Terlevich, R. 1981, *PASP*, **93**, 5
- Caglar, T., Burtcher, L., Brandl, B., et al. 2020, *A&A*, **634**, A114
- Callanan, D., Longmore, S. N., Kruijssen, J. M. D., et al. 2021, *MNRAS*, **505**, 4310
- Calzetti, D. 2001, *PASP*, **113**, 1449
- Calzetti, D. 2013, in *Secular Evolution of Galaxies*, ed. J. Falcón-Barroso & J. H. Knapen (Cambridge: Cambridge Univ. Press), 419
- Calzetti, D., Armus, L., Bohlin, R. C., et al. 2000, *ApJ*, **533**, 682
- Cappellari, M., & Emsellem, E. 2004, *PASP*, **116**, 138
- Cardelli, J. A., Clayton, G. C., & Mathis, J. S. 1989, *ApJ*, **345**, 245
- Comerón, S., Knapen, J. H., Beckman, J. E., et al. 2010, *MNRAS*, **402**, 2462
- Comerón, S., Salo, H., Laurikainen, E., et al. 2014, *A&A*, **562**, A121
- D'Agostino, J. J., Poetrodjojo, H., Ho, I. T., et al. 2018, *MNRAS*, **479**, 4907
- Davies, R. I., Maciejewski, W., Hicks, E. K. S., et al. 2014, *ApJ*, **792**, 101
- Fabian, A. C. 2012, *ARA&A*, **50**, 455
- Fazeli, N., Busch, G., Valencia-S., M., et al. 2019, *A&A*, **622**, A128
- Feltre, A., Charlot, S., & Gutkin, J. 2016, *MNRAS*, **456**, 3354
- Ferland, G. J., Chatzikos, M., Guzmán, F., et al. 2017, *RMxAA*, **53**, 385
- Ferrarese, L., & Merritt, D. 2000, *ApJL*, **539**, L9
- Galliano, E., Alloin, D., Pantin, E., Lagage, P. O., & Marco, O. 2005, *A&A*, **438**, 803
- Gao, Y., Egusa, F., Liu, G., et al. 2021, *ApJ*, **913**, 139
- García-Bernete, I., Alonso-Herrero, A., García-Burillo, S., et al. 2021, *A&A*, **645**, A21
- Gordon, K. D., Clayton, G. C., Misselt, K. A., Landolt, A. U., & Wolff, M. J. 2003, *ApJ*, **594**, 279
- Greene, J. E., Zakamska, N. L., Ho, L. C., & Barth, A. J. 2011, *ApJ*, **732**, 9
- Guainazzi, M., Risaliti, G., Nucita, A., et al. 2009, *A&A*, **505**, 589
- Harrison, C. M. 2017, *NatAs*, **1**, 0165
- Hjelm, M., & Lindblad, P. O. 1996, *A&A*, **305**, 727
- Ho, L. C., Greene, J. E., Filippenko, A. V., & Sargent, W. L. W. 2009, *ApJS*, **183**, 1
- Jorsater, S., & van Moorsel, G. A. 1995, *AJ*, **110**, 2037
- Kennicutt, R. C. J. 1998, *ApJ*, **498**, 541
- King, A., & Pounds, K. 2015, *ARA&A*, **53**, 115
- Kormendy, J., & Ho, L. C. 2013, *ARA&A*, **51**, 511
- Kormendy, J., & Richstone, D. 1995, *ARA&A*, **33**, 581
- Kulkarni, S. R. 2022, *PASP*, **134**, 084302
- Lang, D., Hogg, D. W., Mierle, K., Blanton, M., & Roweis, S. 2010, *AJ*, **139**, 1782
- Leitherer, C., Schaerer, D., Goldader, J. D., et al. 1999, *ApJS*, **123**, 3
- Lena, D., Robinson, A., Storchi-Bergmann, T., et al. 2016, *MNRAS*, **459**, 4485
- Lindblad, P. O. 1999, *A&ARv*, **9**, 221
- Liu, D., Schinnerer, E., Cao, Y., et al. 2023, *ApJL*, **944**, L19
- Magorrian, J., Tremaine, S., Richstone, D., et al. 1998, *AJ*, **115**, 2285
- Maiolino, R., Gallerani, S., Neri, R., et al. 2012, *MNRAS*, **425**, L66
- Moon, S., Kim, W.-T., Kim, C.-G., & Ostriker, E. C. 2021, *ApJ*, **914**, 9
- Moon, S., Kim, W.-T., Kim, C.-G., & Ostriker, E. C. 2022, *ApJ*, **925**, 99
- Nesvadba, N. P. H., Bicknell, G. V., Mukherjee, D., & Wagner, A. Y. 2020, *A&A*, **639**, L13
- Obied, G., Zakamska, N. L., Wylezalek, D., & Liu, G. 2016, *MNRAS*, **456**, 2861
- Osterbrock, D. E., & Ferland, G. J. 2006, *Astrophysics of Gaseous Nebulae and Active Galactic Nuclei* (Sausalito, CA: Univ. Science Books)
- Phillips, M. M., Turtle, A. J., Edmunds, M. G., & Pagel, B. E. J. 1983, *MNRAS*, **203**, 759
- Rupke, D. S., Veilleux, S., & Sanders, D. B. 2002, *ApJ*, **570**, 588
- Sandqvist, A., Hjalmarsen, A., Larsson, B., et al. 2021, *A&A*, **647**, A86
- Schinnerer, E., Emsellem, E., Henshaw, J. D., et al. 2023, *ApJL*, **944**, L15
- Schlafly, E. F., & Finkbeiner, D. P. 2011, *ApJ*, **737**, 103
- Sextl, E., Kudritzki, R.-P., Burkert, A., et al. 2024, *ApJ*, **960**, 83
- Shimizu, T. T., Davies, R. I., Lutz, D., et al. 2019, *MNRAS*, **490**, 5860
- Shin, J., Woo, J.-H., Chung, A., et al. 2019, *ApJ*, **881**, 147
- Singh, K. P. 2022, in *Handbook of X-ray and Gamma-ray Astrophysics*, ed. C. Bambi & A. Santangelo (Singapore: Springer), 83
- Sormani, M. C., Barnes, A. T., Sun, J., et al. 2023, *MNRAS*, **523**, 2918
- Sormani, M. C., Tress, R. G., Glover, S. C. O., et al. 2020, *MNRAS*, **497**, 5024
- Tandon, S. N., Subramaniam, A., Girish, V., et al. 2017, *AJ*, **154**, 128
- Tody, D. 1986, *Proc. SPIE*, **627**, 733
- Valencia-S., M., Zuther, J., Eckart, A., et al. 2012, *A&A*, **544**, A129
- Veilleux, S., & Osterbrock, D. E. 1987, *ApJS*, **63**, 295
- Venturi, G., Nardini, E., Marconi, A., et al. 2018, *A&A*, **619**, A74
- Wang, J., Fabbiano, G., Elvis, M., et al. 2009, *ApJ*, **694**, 718
- Whitmore, B. C., Chandar, R., Rodríguez, M. J., et al. 2023, *ApJL*, **944**, L14
- Zakamska, N. L., & Greene, J. E. 2014, *MNRAS*, **442**, 784
- Zakamska, N. L., Hamann, F., Pâris, I., et al. 2016, *MNRAS*, **459**, 3144
- Zakamska, N. L., Schmidt, G. D., Smith, P. S., et al. 2005, *AJ*, **129**, 1212
- Zubovas, K., Nayakshin, S., King, A., & Wilkinson, M. 2013, *MNRAS*, **433**, 3079